

# Highly coupled MnO<sub>2</sub>/Mn<sub>5</sub>O<sub>8</sub> Z-scheme heterojunction modified by Co<sub>3</sub>O<sub>4</sub> co-catalyst: An efficient and stable photocatalyst to decompose gaseous benzene

Liang Qi<sup>a</sup>, Yangzheng Liu<sup>a</sup>, Yuanqing Tang<sup>a</sup>, Xinyue Jiang<sup>a</sup>, Fei Xie<sup>a</sup>, Lili Wan<sup>b</sup>, Zhongli Wang<sup>a,c</sup>, Xiaojing Wang<sup>b,\*</sup>, Changwei Lü<sup>a,d,\*\*</sup>

<sup>a</sup> Ministry of Education Key Laboratory of Ecology and Resources Use of the Mongolian Plateau, School of Ecology and Environment, Inner Mongolia University, Hohhot 010021, China

<sup>b</sup> Inner Mongolia Key Laboratory of Chemistry and Physics of Rare Earth Materials, School of Chemistry and Chemical Engineering, Inner Mongolia University, Hohhot, Inner Mongolia 010021, China

<sup>c</sup> Faculty of Engineering, University of Nottingham, University Park, Nottingham NG7 2RD, United Kingdom

<sup>d</sup> Institute of Environmental Geology, Inner Mongolia University, Hohhot 010021, China



## ARTICLE INFO

### Keywords:

MnO<sub>x</sub>/Mn<sub>5</sub>O<sub>8</sub> heterojunction  
Co<sub>3</sub>O<sub>4</sub> co-catalyst  
Electrodeposition  
Photocatalytic benzene degradation  
Photocorrosion

## ABSTRACT

MnO<sub>x</sub> Z-scheme heterojunction exhibits a strong redox capacity, thereby it has great potential in the field of photocatalysis for gaseous benzene oxidation to address environmental pollution. However, the self-oxidation of MnO<sub>x</sub> due to the accumulation of photogenerated holes severely restricts its practical application. Herein, a highly coupled MnO<sub>2</sub>/Mn<sub>5</sub>O<sub>8</sub> Z-scheme heterojunction modified by Co<sub>3</sub>O<sub>4</sub> co-catalyst grown on ammoniated carbon cloth (MnO<sub>x</sub>/Co<sub>3</sub>O<sub>4</sub>@ACC) was constructed through electrodeposition and applied for efficient photocatalytic benzene degradation. The optimized MnO<sub>x</sub>/Co<sub>3</sub>O<sub>4</sub>@ACC presents high-efficient degradability, mineralization rate and high stability after 60 cycles (30 h). Co<sub>3</sub>O<sub>4</sub> served as a hole collector to promote the extraction of photogenerated holes from the MnO<sub>x</sub> surface, suppressing the photocorrosion of MnO<sub>x</sub>. Additionally, the by-product CO was more easily absorbed and activated on MnO<sub>x</sub>/Co<sub>3</sub>O<sub>4</sub>@ACC surface due to the introduction of Co<sub>3</sub>O<sub>4</sub>. The electrodeposition-photocatalysis strategy developed in this work shows great application prospects for environmental contaminant remediation.

## 1. Introduction

Benzene series, a kind of chemical raw materials, are widely used in construction, decoration materials, paints and petrochemical plants [1, 2]. However, the excessive utilization of benzene causes serious environmental and health problems due to its volatility and toxicity. It would form near-surface ozone and photochemical smog, atmospheric toxicity and carcinogenic effects, which hazard human health [3]. Photocatalytic oxidation of benzene can efficiently convert benzene into carbon dioxide (CO<sub>2</sub>) and water (H<sub>2</sub>O) under solar light illumination, representing a promising strategy for mitigating the atmospheric environmental problem and achieving renewable energy utilization goals [4, 5]. Manganese oxides (MnO, Mn<sub>2</sub>O<sub>3</sub>, MnO<sub>2</sub>, Mn<sub>3</sub>O<sub>4</sub>, Mn<sub>5</sub>O<sub>8</sub>), as one of

numerous transition metal oxide families, are regarded as a promising photocatalytic material [6–9] owing to their suitable band gap, strong light absorption capacity and redox capacity. The formation of the Z-scheme heterostructure of different MnO<sub>x</sub> has been demonstrated to be effective in reducing the photogenerated carrier recombination and improving the photocatalytic activity [10,11]. Recent studies have elucidated that MnO<sub>x</sub> Z-scheme heterojunction facilitates charge transfers at the interfaces due to its uniform composition and strong built-in electric field [10]. Meanwhile, MnO<sub>x</sub> Z-scheme heterojunction can enhance electron transfer capability and improve light absorption by tuning the bandgap, and introducing interfaces to show excellent lattice matching [12]. However, most MnO<sub>x</sub> photocatalysts suffer from crystal oxidation and photocorrosion in pollutant degradation processes.

\* Corresponding author.

\*\* Corresponding author at: Ministry of Education Key Laboratory of Ecology and Resources Use of the Mongolian Plateau, School of Ecology and Environment, Inner Mongolia University, Hohhot 010021, China.

E-mail addresses: [wang\\_xiao\\_jing@hotmail.com](mailto:wang_xiao_jing@hotmail.com) (X. Wang), [lcw2008@imu.edu.cn](mailto:lcw2008@imu.edu.cn) (C. Lü).

Firstly, photo-excited holes ( $\text{h}^+$ ) in the valence band (VB) gradually oxidize  $\text{Mn}^{\text{III}}$  or  $\text{Mn}^{\text{II}}$  to  $\text{Mn}^{\text{IV}}$  in  $\text{MnO}_x$ . Moreover, continuous photocorrosion damages the  $\text{MnO}_x$  crystal, leading to structural instability and catalyst deactivation [13].

To overcome the tough issues of photocorrosion and structural instability, the co-catalyst has been introduced as a hole collector to facilitate the extraction of photogenerated holes from the surface of  $\text{MnO}_x$ . This effectively stabilizes the valence state of Mn in  $\text{MnO}_x$  and improves its stability [14,15]. The tricobalt tetraoxide ( $\text{Co}_3\text{O}_4$ ) has been demonstrated as an excellent co-catalyst for holes collection. It not only reduces the interfacial resistance, but also greatly improves photocorrosion resistance during photocatalytic pollutant degradation [16–18]. Inspired by the above discussion, the introduction of  $\text{Co}_3\text{O}_4$  co-catalyst into  $\text{MnO}_2/\text{Mn}_5\text{O}_8$  Z-scheme heterojunction might effectively address the stability problem of Mn-based photocatalysts. Besides, appropriate work function and low hole transfer overpotentials make  $\text{Co}_3\text{O}_4$  easy to integrate well with  $\text{MnO}_x$ . Even so, the unsatisfactory stability of  $\text{MnO}_x$  photocatalysts still cannot be solved in some cases. For example, traditional synthesis methods, including hydrothermal [4,19] and coprecipitation [20,21] methods, cause the high interface resistance and the lack of effective oxidation centers [9,22]. Therefore, it is of great significance to construct  $\text{MnO}_x/\text{Co}_3\text{O}_4$  through reasonable design to optimize the interface electron transport properties.

The electrodeposition strategy on the carbon cloth provides an effective method to solve the above problem, playing an important role in cost-effective and industrial applications [23]. Firstly, the ammoniated carbon cloth (ACC) surface captures benzene well at the pre-enriched procedure [24]. Secondly, the highly coupled  $\text{MnO}_x$  Z-scheme heterojunction structure is easily formed to effectively restrain the recombination of electron-holes. Thirdly, the  $\text{Co}_3\text{O}_4$  co-catalyst can extract photogenerated holes from the surface of  $\text{MnO}_x$ , which may help to alleviate  $\text{MnO}_x$  photocorrosion from the oxidation by holes. Therefore, the efficient and stable photocatalyst on the carbon cloth surface obtained by electrodeposition is a worthy attempt.

Herein, a highly coupled  $\text{MnO}_2/\text{Mn}_5\text{O}_8$  ( $\text{MnO}_x$ ) Z-scheme heterojunction on ammoniated carbon cloth (ACC) surface was constructed via a simple electrodeposition method. The component ratio of  $\text{MnO}_2$  and  $\text{Mn}_5\text{O}_8$  was optimized by controlling the potential to achieve great catalytic performance. To solve the photocorrosion and structural instability of  $\text{MnO}_x$  Z-scheme heterojunction,  $\text{Co}_3\text{O}_4$  co-catalyst was further loaded through the “step-by-step deposition-growing” to optimize the electron transfer pathway (Fig. S1 and S2). Based on characterization results and gaseous benzene degradation experiments, the photocorrosion resistance mechanism was proposed. This work provides a novel design idea for the photocatalyst aiming to enhance the rapid decomposition ability of benzene and its durable stability in gas-solid systems, promoting its practical application in different scenarios.

## 2. Materials and preparation

### 2.1. Materials

All the reagents used for the catalyst synthesis are analytical reagents grade, which can be used directly without further purification. Manganese (II) nitrate tetrahydrate ( $\text{Mn}(\text{NO}_3)_2 \cdot 4 \text{ H}_2\text{O}$ , 99.0 %), Manganese (II) acetate tetrahydrate ( $\text{Mn}(\text{CH}_3\text{COO})_2 \cdot 4 \text{ H}_2\text{O}$ , 99.0 %), cobalt nitrate hexahydrate ( $\text{Co}(\text{NO}_3)_2 \cdot 6 \text{ H}_2\text{O}$ , 99.0 %), cobalt (II) acetate tetrahydrate ( $\text{Co}(\text{CH}_3\text{COO})_2 \cdot 4 \text{ H}_2\text{O}$ , 98.0 %), benzene ( $\text{C}_6\text{H}_6$ , 99.5 %) and carbon cloth (CC, thickness: 330  $\mu\text{m}$ ) were purchased from Inno Chem (Beijing) Technology Co., Ltd. Ammonia solution ( $\text{NH}_3$ , 25.0 %–30.0 % in water), acetone and ethanol were bought from Sinopharm Chemical Reagent Co., Ltd. The water used in all experiments was deionized water.

### 2.2. Preparation of alkali-etched carbon cloth substrate (ACC)

Firstly, the carbon cloth (CC, 2  $\times$  2 cm) was sequentially cleaned by ultrasonication in acetone, ethanol and deionized water for 20 min, respectively. Next, the dried CC was immersed in ammonia water (30.0 %) for 24 h. After washing and drying, an alkali-etched carbon cloth denoted as ACC, was obtained.

### 2.3. Preparation of $\text{MnO}_2/\text{Mn}_5\text{O}_8$ heterojunction on ACC surface ( $\text{MnO}_x@\text{ACC}$ )

The mixture included 2.5 mmol  $\text{Mn}(\text{NO}_3)_2 \cdot 4 \text{ H}_2\text{O}$  and 2.5 mmol  $\text{Mn}(\text{CH}_3\text{COO})_2 \cdot 4 \text{ H}_2\text{O}$  were used as reactants, which were fully dissolved in 50 mL of deionized water under stirring to obtain the electrolytes. Next, a three-electrode system containing an ACC as a working electrode, Pt plate as a counter electrode, and Ag/AgCl as a reference electrode were utilized for the deposition of manganese hydroxides at different potentials (-1.1 V, -1.3 V, -1.5 V and -1.7 V) for 3000 s at room temperature. Finally,  $\text{MnO}_x@\text{ACC}$  was obtained by calcination at 400 °C for 2 h. The resulting samples were denoted as  $\text{MnO}_x@\text{ACC}-1.1$ ,  $\text{MnO}_x@\text{ACC}-1.3$ ,  $\text{MnO}_x@\text{ACC}-1.5$  and  $\text{MnO}_x@\text{ACC}-1.7$ , according to the different deposition potentials.

### 2.4. Preparation of $\text{MnO}_2/\text{Mn}_5\text{O}_8/\text{Co}_3\text{O}_4$ on ACC surface ( $\text{MnO}_x/\text{Co}_3\text{O}_4@\text{ACC}$ )

Mn hydroxide with a -1.5 V deposition potential in Section 2.3 was immersed into 50 mL of fully dissolved mixed  $\text{Co}(\text{NO}_3)_2 \cdot 6 \text{ H}_2\text{O}$  (2.5 mmol) and  $\text{Co}(\text{CH}_3\text{COO})_2 \cdot 4 \text{ H}_2\text{O}$  (2.5 mmol) solution, and exerted a constant current density of -5 mA/cm<sup>2</sup> for 800 s to obtain Mn/Co hydroxide. Finally,  $\text{MnO}_x/\text{Co}_3\text{O}_4@\text{ACC}$  was obtained after calcination under air at 400 °C for 2 h. The  $\text{Co}_3\text{O}_4@\text{ACC}$  was prepared by depositing Co hydroxide on ACC directly under the same current density and calcination condition. The deposition mass of the as-prepared samples was shown in Table S1.

## 3. Results and discussion

### 3.1. Structure and morphology

The X-ray diffraction (XRD) patterns of the prepared samples were shown in Fig. 1a. The diffraction peaks of CC and ACC at 25.8° and 43.3° belonged to carbon (JCPDS 075–1621). The diffraction peaks appearing on  $\text{MnO}_x@\text{ACC}-1.5$  was assigned to  $\text{MnO}_2$  and  $\text{Mn}_5\text{O}_8$ , indicating a mixed phase of  $\text{MnO}_x$  on  $\text{MnO}_x@\text{ACC}-1.5$ . Besides, the crystal phases of the manganese oxide can be controlled with the different deposition potentials (Fig. S3). Similarly,  $\text{Co}_3\text{O}_4$  in  $\text{Co}_3\text{O}_4@\text{ACC}$  was assigned to the cubic structure (JCPDS 900–5891). The peaks of  $\text{MnO}_2$ ,  $\text{Mn}_5\text{O}_8$  and  $\text{Co}_3\text{O}_4$  were all observed on  $\text{MnO}_x/\text{Co}_3\text{O}_4@\text{ACC}$ , demonstrating the co-existence of Mn and Co oxides on the ACC surface. The functional groups of the ACC were investigated through fourier transform infrared spectra (FT-IR) analysis. As shown in Fig. S4a, it is evident that nitrogen-containing functional groups were successfully incorporated on the surface of the ACC compared with CC. Notably, the strong capture capacity of benzene on the ACC surface can be attributed to the increased surface roughness (Fig. S4b–e). The FT-IR spectra of  $\text{MnO}_x/\text{Co}_3\text{O}_4@\text{ACC}$  also confirmed the co-existence of manganese oxide and cobaltous oxide on the ACC surface (Fig. S5) owing to the presence of Mn–O [25] and Co–O [26] stretching modes. The UV–vis diffuse reflectance spectrum (UV–vis DRS) was used to study the optical absorption properties of the samples. As shown in Fig. S6a, the light-absorbing ability of black  $\text{MnO}_x$  was significantly expanded from UV to visible light and even to the infrared region after calcination treatment. Therefore, all the synthesized materials in the present work exhibited good light absorption. Compared to  $\text{MnO}_x@\text{ACC}-1.1$  and  $\text{MnO}_x@\text{ACC}-1.7$ ,  $\text{MnO}_x@\text{ACC}-1.5$  had nearly 95 % light absorption in the visible light region, indicating a

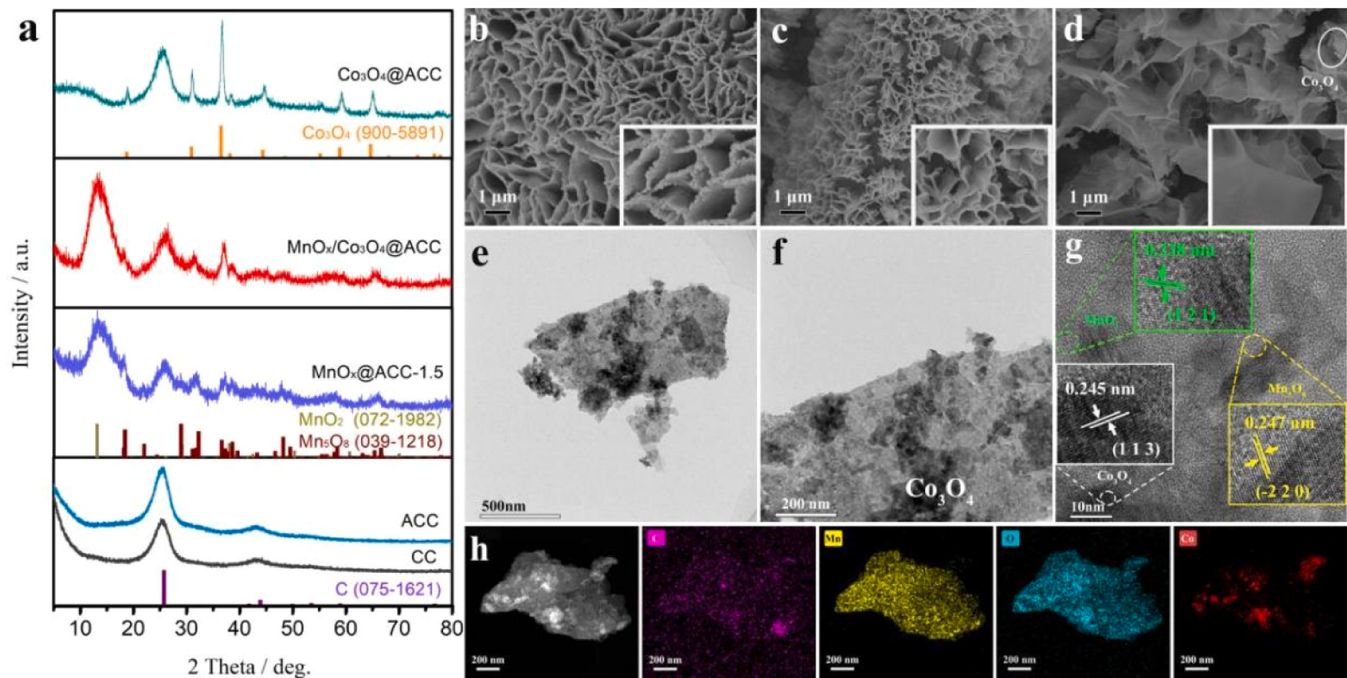


**Fig. 1.** (a) The XRD patterns of CC and ACC,  $\text{MnO}_x$ @ACC-1.5,  $\text{MnO}_x/\text{Co}_3\text{O}_4$ @ACC. SEM images of (b)  $\text{MnO}_x$ @ACC-1.5, (c)  $\text{Co}_3\text{O}_4$ @ACC, (d)  $\text{MnO}_x/\text{Co}_3\text{O}_4$ @ACC, (e, f, g) TEM images of  $\text{MnO}_x/\text{Co}_3\text{O}_4$ @ACC, (h) EDS mapping images of  $\text{MnO}_x/\text{Co}_3\text{O}_4$ @ACC.

significantly enhanced photo-correspondence ability due to the  $\text{MnO}_2/\text{Mn}_5\text{O}_8$  heterojunction. After the induction of  $\text{Co}_3\text{O}_4$ , the UV-vis DRS of  $\text{MnO}_x/\text{Co}_3\text{O}_4$ @ACC presented an ultrahigh light absorption across the whole solar spectrum, especially in the infrared region (Fig. S6b). Evidently, the enhanced infrared light absorption of  $\text{MnO}_x/\text{Co}_3\text{O}_4$ @ACC was attributed to the incorporation of  $\text{Co}_3\text{O}_4$ , which benefited the photocatalytic reaction.

The morphologies of the as-prepared samples were investigated using scanning electron microscope (SEM) and transmission electron microscopy (TEM). It can be seen that the ACC surface (Fig. S7c, d) was gradually covered by manganese oxides prepared at different deposition potentials (Fig. S7e-l).  $\text{MnO}_x$ @ACC-1.1 was piled up by scattered  $\text{MnO}_2$  particles, while at other deposition potentials, the  $\text{MnO}_x$  structure displayed an irregular honeycombed morphology caused by the accumulation of many small particles of manganese oxides. The morphology of  $\text{Co}_3\text{O}_4$ @ACC was similar to that of  $\text{MnO}_x$ @ACC-1.5 (Fig. 1c), but no aggregation of small particles at the pleated edge was observed. Moreover, the high-resolution TEM (HR-TEM) image of  $\text{MnO}_x$ @ACC-1.5 shows that the well-defined lattice fringes of 0.238 and 0.247 nm, corresponding to the (1 2 1) plane of  $\text{MnO}_2$  and (-2 2 0) plane of  $\text{Mn}_5\text{O}_8$ , respectively (Fig. S8). This result confirmed that  $\text{MnO}_2$  and  $\text{Mn}_5\text{O}_8$  were successfully combined to form heterojunction.  $\text{MnO}_x/\text{Co}_3\text{O}_4$ @ACC exhibited a fully open structure of scattered petal-like sheets with the coupled  $\text{Co}_3\text{O}_4$  nanoclusters distributed on the surface of  $\text{MnO}_x$  (Fig. 1d, e). This unique open structure enhanced the interfacial effect between  $\text{MnO}_x$  and  $\text{Co}_3\text{O}_4$ , and exposed more reaction sites. The low-magnification TEM images of  $\text{MnO}_x/\text{Co}_3\text{O}_4$ @ACC were in accord with SEM observation (Fig. 1e, f). In addition, the HR-TEM image of  $\text{MnO}_x/\text{Co}_3\text{O}_4$ @ACC (Fig. 1g) showed the coexistence of the crystal plane of  $\text{MnO}_x$  and  $\text{Co}_3\text{O}_4$ . EDS mapping images demonstrated that Mn, Co, O and C elements were evenly dispersed throughout  $\text{MnO}_x/\text{Co}_3\text{O}_4$ @ACC photocatalyst (Fig. 1h). To better understand the structure of  $\text{MnO}_x/\text{Co}_3\text{O}_4$ @ACC in this work, the mole ratios of  $\text{MnO}_2$ ,  $\text{Mn}_5\text{O}_8$  and  $\text{Co}_3\text{O}_4$  were approximately estimated as 0.37:0.51:0.35 using inductively coupled plasma optical emission spectrometry (ICP-OES) analysis and the XRD integral area (Table S2).

### 3.2. Band structure

The energy band structures of  $\text{MnO}_2$  and  $\text{Mn}_5\text{O}_8$  were analyzed by valence band X-ray photoelectron spectroscopy (VB-XPS) and Mott-Schottky plots. The valence bands ( $E_{VB}$ ) of  $\text{MnO}_2$  and  $\text{Mn}_5\text{O}_8$  were calculated to be 1.48 eV, 2.45 eV (vs. NHE), respectively (Fig. S9a), in agreement with the results of  $E_{VB}$  by ultraviolet photoelectron spectrometer (UPS, Fig. S10). The Mott-Schottky plots showed that both materials exhibited positive slopes, indicating their classification as n-type semiconductor (Fig. S9b-c) [27]. The flat-band potentials ( $E_{FB}$ ) of  $\text{MnO}_2$ ,  $\text{Mn}_5\text{O}_8$  were estimated to be -1.26 eV, -0.17 eV (vs. SCE), respectively. In general,  $E_{FB}$  of the n-type semiconductor was 0.1–0.3 V higher than the conduction band potential ( $E_{CB}$ ). Hence, the  $E_{CB}$  of  $\text{MnO}_2$ ,  $\text{Mn}_5\text{O}_8$  was roughly estimated as -1.46 eV, -0.37 eV (vs. SCE), that is, -0.82 eV, 0.27 eV (vs. NHE) ( $E_{NHE} = E_{SCE} + 0.05916 \text{ pH} + 0.241 \text{ V}$ ), respectively [28]. According to the formula  $E_g = E_{VB} - E_{CB}$ , where the  $E_g$  of  $\text{MnO}_2$ ,  $\text{Mn}_5\text{O}_8$  was calculated as 2.30 eV, 2.18 eV, respectively. As shown in Fig. S11, the band gap value of  $\text{MnO}_2$ ,  $\text{Mn}_5\text{O}_8$  was also calculated as 2.30 eV and 2.18 eV using Kubelka-Munk transformation method. Similarly, the  $E_{VB}$  and  $E_{CB}$  of  $\text{Co}_3\text{O}_4$  were calculated as 2.65 eV and 0.80 eV by the same method (Fig. S9d and S11), thus the  $E_g$  of  $\text{Co}_3\text{O}_4$  was calculated to be 1.85 eV. Additionally, the calculated  $E_g$  of  $\text{MnO}_2$ ,  $\text{Mn}_5\text{O}_8$  and  $\text{Co}_3\text{O}_4$  by DFT + U method (Fig. S12) coincided with the experimental results.

### 3.3. Photocatalytic degradation rate and stability test

To assess the degradation of gaseous benzene under solar light, the catalytic activities of the samples were evaluated and the details were listed in Table S1. As shown in Fig. 2a-b, almost no carbon dioxide was detected in the case of only ACC sample or without light irradiation, implying the absence of benzene degradation. Similarly, under solar light, the oxidation of ACC to  $\text{CO}_2$  (20.1 ppm) and CO (1.3 ppm) could be negligible without gaseous benzene when only the ACC sample was present (Fig. S13). Notably,  $\text{MnO}_x$ @ACC-1.5 exhibited an accelerated benzene degradation rate (100 %), mineralization rate (96.8 %) and reduced CO generation rate (0.655 %) in 30 min, surpassing the

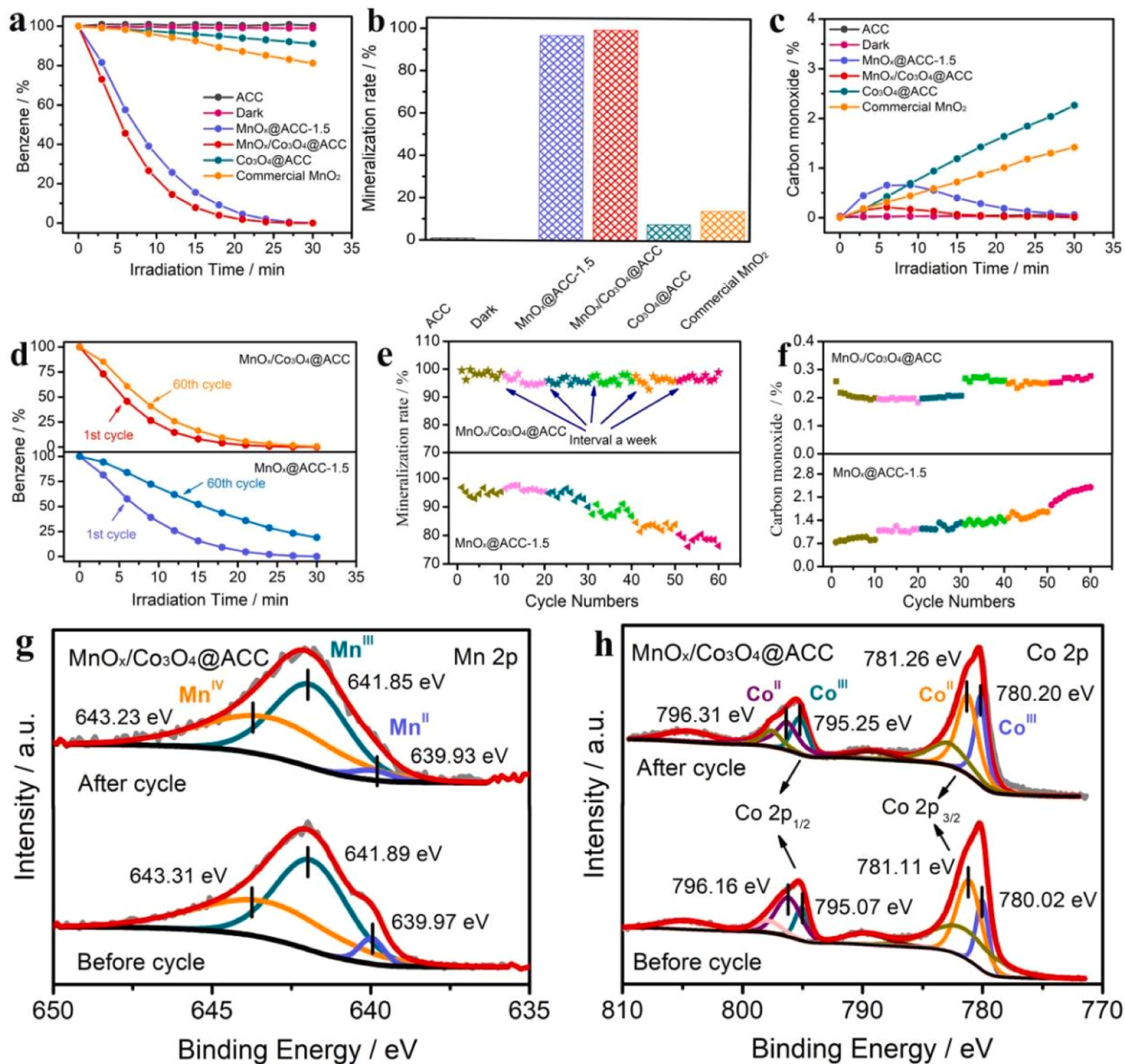


**Fig. 2.** (a) Photocatalytic degradation rate of benzene, (b) mineralization rate, (c) CO generation rate. (d) The photocatalytic benzene degradation rate at the 1st cycle and 60th, (e) mineralization rate, (f) CO generation rate with 60 cycles for MnO<sub>x</sub>@ACC-1.5 and MnO<sub>x</sub>/Co<sub>3</sub>O<sub>4</sub>@ACC in one week interval for every 10 cycles. Comparative XPS of MnO<sub>x</sub>/Co<sub>3</sub>O<sub>4</sub>@ACC before and after cycle: (g) Mn 2p, (h) Co 2p.

performance of the pristine ACC and the other Mn oxides at different potentials (Fig. S14). Thus, the construction of MnO<sub>2</sub>/Mn<sub>5</sub>O<sub>8</sub> heterojunction effectively accelerated the separation and migration of the carriers. Although the construction of MnO<sub>2</sub>/Mn<sub>5</sub>O<sub>8</sub> heterojunction could effectively improve the photocatalytic performance, the high interface resistance still hindered the further degradation of CO [16]. Therefore, Co<sub>3</sub>O<sub>4</sub> as co-catalyst was introduced into MnO<sub>2</sub>/Mn<sub>5</sub>O<sub>8</sub> heterojunction to solve this problem. With the introduction of Co<sub>3</sub>O<sub>4</sub> into MnO<sub>2</sub>/Mn<sub>5</sub>O<sub>8</sub> system, the resulting MnO<sub>x</sub>/Co<sub>3</sub>O<sub>4</sub>@ACC presented a higher mineralization rate (99.6 %) and a lower CO generation rate (0.210 %), far exceeding those of Co<sub>3</sub>O<sub>4</sub>@ACC and commercial MnO<sub>2</sub> (Fig. 2a-c and Fig. S15). Meanwhile, the gas chromatography-mass spectrometry (GC-MS) results also demonstrated a significantly enhanced selectivity of MnO<sub>x</sub>/Co<sub>3</sub>O<sub>4</sub>@ACC towards the conversion of benzene into CO<sub>2</sub> (Fig. S16).

The degradation performances of gaseous benzene on MnO<sub>x</sub>/Co<sub>3</sub>O<sub>4</sub>@ACC were tested at different temperatures without light illumination. Even when the reactor temperature was elevated to 170 °C, an extremely low conversion rate was observed (Fig. S17), suggesting that the exceptional catalytic activity of the samples originated from irradiated light energy. In addition, the photocatalytic degradation ability of MnO<sub>x</sub>/Co<sub>3</sub>O<sub>4</sub>@ACC towards various concentrations of benzene was tested. It was found that even when the benzene concentration was increased to 7500 ppm, the degradation rate remained remarkably high as 98.5 % in 30 min, with a 75 % mineralization rate (Fig. S18). The photocatalytic degradation performance of gaseous benzene was compared with that reported in related studies, as illustrated in Fig. S19 and Table S3. It is evident that MnO<sub>x</sub>/Co<sub>3</sub>O<sub>4</sub>@ACC in this work exhibited outstanding decomposition ability and mineralization rate towards gaseous benzene.

The stability test results of  $\text{MnO}_x@\text{ACC}-1.5$  and  $\text{MnO}_x/\text{Co}_3\text{O}_4@\text{ACC}$  for the degradation of benzene were shown in Fig. 2d-f. Evidently, the photocatalytic activities of  $\text{MnO}_x/\text{Co}_3\text{O}_4@\text{ACC}$  for benzene oxidation remained comparatively excellent performance after 60 cycles. Meanwhile, it was found that  $\text{MnO}_x/\text{Co}_3\text{O}_4@\text{ACC}$  exhibited a stable mineralization rate and lower CO generation rate. In contrast, the benzene degradation rate of  $\text{MnO}_x@\text{ACC}-1.5$  declined from 100 % to 81.15 % after 60 cycles, accompanied by a significant decrease in the mineralization rate and an increase in the CO generation rate.

Additionally, the crystal structures and morphologies of the used  $\text{MnO}_x@\text{ACC}-1.5$  and  $\text{MnO}_x/\text{Co}_3\text{O}_4@\text{ACC}$  were investigated using XRD, SEM, FTIR and photoluminescence (PL). Compared with the XRD patterns of the fresh  $\text{MnO}_x/\text{Co}_3\text{O}_4@\text{ACC}$ , the peak intensity of  $\text{MnO}_2$  (denote as ♦) at 12.7° slightly decreased, and the peak intensity of  $\text{Mn}_5\text{O}_8$  (denote as ♥) exhibited a subtle increase (Fig. S20d) for the used  $\text{MnO}_x/\text{Co}_3\text{O}_4@\text{ACC}$ . Surprisingly, the structure of the used  $\text{MnO}_x@\text{ACC}-1.5$  was destroyed and the diffraction peak of  $\text{MnO}_2$  at 12.7° almost disappeared, whilst the peak intensity of  $\text{Mn}_5\text{O}_8$  was stronger (Fig. S20a). Additionally, no significant changes were observed in the SEM images (Fig. S20e-f) and FT-IR pattern (Fig. S21b) and PL spectra (Fig. S21d) of the used  $\text{MnO}_x/\text{Co}_3\text{O}_4@\text{ACC}$ , suggesting that the introduction of  $\text{Co}_3\text{O}_4$  facilitated the extraction of photogenerated holes from  $\text{MnO}_x$  and effectively inhibited its self-oxidation to a certain extent. In contrast, the SEM images (Fig. S20b-c) revealed increased particles size for the used  $\text{MnO}_x@\text{ACC}-1.5$ , while the FT-IR pattern (Fig. S21a) exhibited a significantly weaker peak intensity at  $516 \text{ cm}^{-1}$  and a marked enhancement in PL signal (Fig. S21c). Obviously,  $\text{MnO}_x$  in the used  $\text{MnO}_x@\text{ACC}-1.5$  experienced photocorrosion due to the accumulation of excessive photo-induced holes on its surface.

To gain deeper insights into the stability differences of the catalysts, X-ray photoelectron spectroscopy (XPS) analysis was performed on the used  $\text{MnO}_x@\text{ACC}-1.5$  and  $\text{MnO}_x/\text{Co}_3\text{O}_4@\text{ACC}$ . The Mn 2p peak can be deconvoluted into three peaks for used  $\text{MnO}_x@\text{ACC}-1.5$  (Fig. S22) and  $\text{MnO}_x/\text{Co}_3\text{O}_4@\text{ACC}$  (Fig. 2g). The binding energies (BEs) were associated to  $\text{Mn}^{II}$ ,  $\text{Mn}^{III}$ ,  $\text{Mn}^{IV}$  from low to high, respectively. Among the existing manganese species, the  $\text{Mn}^{II}$ ,  $\text{Mn}^{III}$  proportions of the used  $\text{MnO}_x@\text{ACC}-1.5$  decreased significantly, while the  $\text{Mn}^{IV}$  proportion of the used  $\text{MnO}_x@\text{ACC}-1.5$  increased (Table S4), indicating that photogenerated holes in  $\text{MnO}_x$  surface oxidized  $\text{Mn}^{II}$  and  $\text{Mn}^{III}$  into  $\text{Mn}^{IV}$ . After the introduction of  $\text{Co}_3\text{O}_4$ , despite a slight decrease in the proportion of  $\text{Mn}^{II}$  due to the oxidation of photogenerated holes, the fitting peak areas of  $\text{Mn}^{III}$  and  $\text{Mn}^{IV}$  remained stable for the used  $\text{MnO}_x/\text{Co}_3\text{O}_4@\text{ACC}$  in the present system (Fig. 2g and Table S4). The fitting peaks position of Co 2p in the used  $\text{MnO}_x/\text{Co}_3\text{O}_4@\text{ACC}$  shifted towards higher binding energy compared to that of the fresh  $\text{MnO}_x/\text{Co}_3\text{O}_4@\text{ACC}$ , implying a reduction in electron density after cycles. Moreover, the peak areas of  $\text{Co}^{II}$  and  $\text{Co}^{III}$  in the used  $\text{MnO}_x/\text{Co}_3\text{O}_4@\text{ACC}$  were also similar with the fresh  $\text{MnO}_x/\text{Co}_3\text{O}_4@\text{ACC}$  (Fig. 2h). These results mentioned above testify that the stability test has no influence on the valence of  $\text{Co}_3\text{O}_4$ , which was significant for improving the stability of  $\text{MnO}_x$ . Overall,  $\text{MnO}_x/\text{Co}_3\text{O}_4@\text{ACC}$  as a promising photocatalytic material exhibited remarkable catalytic activity and stability. It can adapt to the degradation of gaseous benzene at various concentrations, which showed a potential environmental remediation capacity.

### 3.4. Photocatalytic decontamination mechanism

#### 3.4.1. The enhanced transport and separation of the photo-excited electron-hole pairs

PL spectra was widely used to analyze the separation of photogenerated electrons and holes [29]. As presented in Fig. S23a, the PL signal of  $\text{MnO}_2/\text{Mn}_5\text{O}_8$  heterojunction was significantly lower compared to that of single-phase structure. It was reasonable to speculate that the new channel generated by the interface contact between  $\text{MnO}_2$  and  $\text{Mn}_5\text{O}_8$  improved the ability of the electrons transfer, and avoided the recombining of the photogenerated electrons and holes. After  $\text{Co}_3\text{O}_4$  was

introduced into  $\text{MnO}_2/\text{Mn}_5\text{O}_8$  heterojunction, the lowest PL signal of  $\text{MnO}_x/\text{Co}_3\text{O}_4@\text{ACC}$  was observed, indicating that the interaction between  $\text{Co}_3\text{O}_4$  co-catalyst and  $\text{MnO}_x$  greatly restrained the recombination of carriers (Fig. 3a). Furthermore, the time-resolved fluorescence decay spectroscopy (TRPL) reflected the photogenerated carrier lifetime of  $\text{MnO}_x@\text{ACC}-1.5$  and  $\text{MnO}_x/\text{Co}_3\text{O}_4@\text{ACC}$ . According to TRPL results (Fig. 3b and Table S5),  $\text{MnO}_x/\text{Co}_3\text{O}_4@\text{ACC}$  revealed a longer average lifetime ( $\tau_{avg}$ ) than that of  $\text{MnO}_x@\text{ACC}-1.5$ , illustrating that the introduction of  $\text{Co}_3\text{O}_4$  co-catalyst could help prolong the lifetime of charges.

The transport efficiency of photogenerated carriers was further investigated using transient photocurrent. It can be seen from Fig. S23b that  $\text{MnO}_x@\text{ACC}-1.5$  photocatalyst presented a higher stable photocurrent value in several light on-off cycles, indicating that the  $\text{MnO}_2/\text{Mn}_5\text{O}_8$  heterojunction promoted the rapid transfer of the photogenerated electrons at the interface. Once  $\text{Co}_3\text{O}_4$  was introduced into  $\text{MnO}_2/\text{Mn}_5\text{O}_8$  heterojunction, the photocurrent of  $\text{MnO}_x/\text{Co}_3\text{O}_4@\text{ACC}$  was remarkably enhanced under full spectrum irradiation, with an increase of approximately 1.1 times compared to that of  $\text{MnO}_x@\text{ACC}-1.5$  and 2.1 times compared to that of  $\text{Co}_3\text{O}_4@\text{ACC}$  (Fig. 3c). This result demonstrated that  $\text{Co}_3\text{O}_4$  co-catalyst effectively improved the separation and migration of carriers. Furthermore, the electron transfer efficiency was measured by electrochemical impedance spectroscopy (EIS). Since  $\text{MnO}_2/\text{Mn}_5\text{O}_8$  heterojunction facilitated the transfer of photogenerated electrons, the arc radius of  $\text{MnO}_x@\text{ACC}-1.5$  was the smaller compared to  $\text{MnO}_x@\text{ACC}-1.1$  and  $\text{MnO}_x@\text{ACC}-1.7$  (Fig. S23c). After the introduction of  $\text{Co}_3\text{O}_4$ ,  $\text{MnO}_x/\text{Co}_3\text{O}_4@\text{ACC}$  possessed the smallest arc radius among these photocatalysts, confirming that accelerated photo-induced charge carriers separation and fast interfacial charge migration were achieved by aid of  $\text{Co}_3\text{O}_4$  on  $\text{MnO}_x$  surface. (Fig. 3d).

The carrier diffusion and recombination processes in the samples were investigated by the surface photovoltage (SPV) method (Fig. S24a). A built-in electric field directing from the bulk phase to the surface was formed due to upward band bending at the n-type semiconductor surface, thus the holes were driven to the surface by internal electric field.  $\text{MnO}_x@\text{ACC}-1.5$  photocatalyst showed a weaker SPV signal intensity, indicating a smaller number of holes being transmitted to the surface. The SPV signal intensity of  $\text{MnO}_x/\text{Co}_3\text{O}_4@\text{ACC}$  photocatalyst distinctly increased upon the incorporation of  $\text{Co}_3\text{O}_4$  for holes extraction from  $\text{MnO}_x$ , indicating that holes transfer by  $\text{Co}_3\text{O}_4$  was the main driving force for the extraction of photogenerated holes in  $\text{MnO}_x/\text{Co}_3\text{O}_4@\text{ACC}$ , thereby contributing to the improvement of photocatalytic stability. This further validated the reason for the enhanced PL, transient photocurrents and EIS results of  $\text{MnO}_x/\text{Co}_3\text{O}_4@\text{ACC}$ . Moreover, photocurrent-potential curves of  $\text{MnO}_x@\text{ACC}-1.5$  and  $\text{MnO}_x/\text{Co}_3\text{O}_4@\text{ACC}$  were acquired under illumination in Fig. S24b. The photocurrent density detected from  $\text{MnO}_x/\text{Co}_3\text{O}_4@\text{ACC}$  was up to  $-0.71 \text{ mA/cm}^2$  at 0 V vs. RHE, which increased about 2.73 times compared to  $\text{MnO}_x@\text{ACC}-1.5$  ( $-0.26 \text{ mA/cm}^2$ ). This result could be attribute to the fast separation and transportation of photogenerated electron-hole pairs in  $\text{MnO}_x/\text{Co}_3\text{O}_4@\text{ACC}$ , which was benefited from the benign hole trapping ability of  $\text{Co}_3\text{O}_4$ . In view of the above findings, it can be reasonably inferred that  $\text{Co}_3\text{O}_4$  reduced the charge transfer barrier at the interface and extracted the photogenerated holes form  $\text{MnO}_x$  surface, suppressed the photocorrosion issue of  $\text{MnO}_x$  and promoted the overall photocatalytic oxidation properties.

#### 3.4.2. $\text{MnO}_2$ and $\text{Mn}_5\text{O}_8$ Z-scheme heterostructure and electron transfer pathway

Since the interfacial charge transfer process was close relevant to the work functions (W) of the samples, the W of  $\text{MnO}_2$  and  $\text{Mn}_5\text{O}_8$  were calculated using UPS (Fig. S10), which were determined to be 4.21 eV and 5.27 eV, respectively. Obviously,  $\text{Mn}_5\text{O}_8$  exhibited a lower Fermi level ( $E_F$ ) than  $\text{MnO}_2$  before they contact (Fig. 4a). When  $\text{MnO}_2$  and  $\text{Mn}_5\text{O}_8$  were in close contact, the free electrons would be transferred from the higher ( $\text{MnO}_2$ ) to the lower ( $\text{Mn}_5\text{O}_8$ )  $E_F$ , which created an internal electric field (IEF) and energy band edge bending at  $\text{MnO}_2/\text{Mn}_5\text{O}_8$

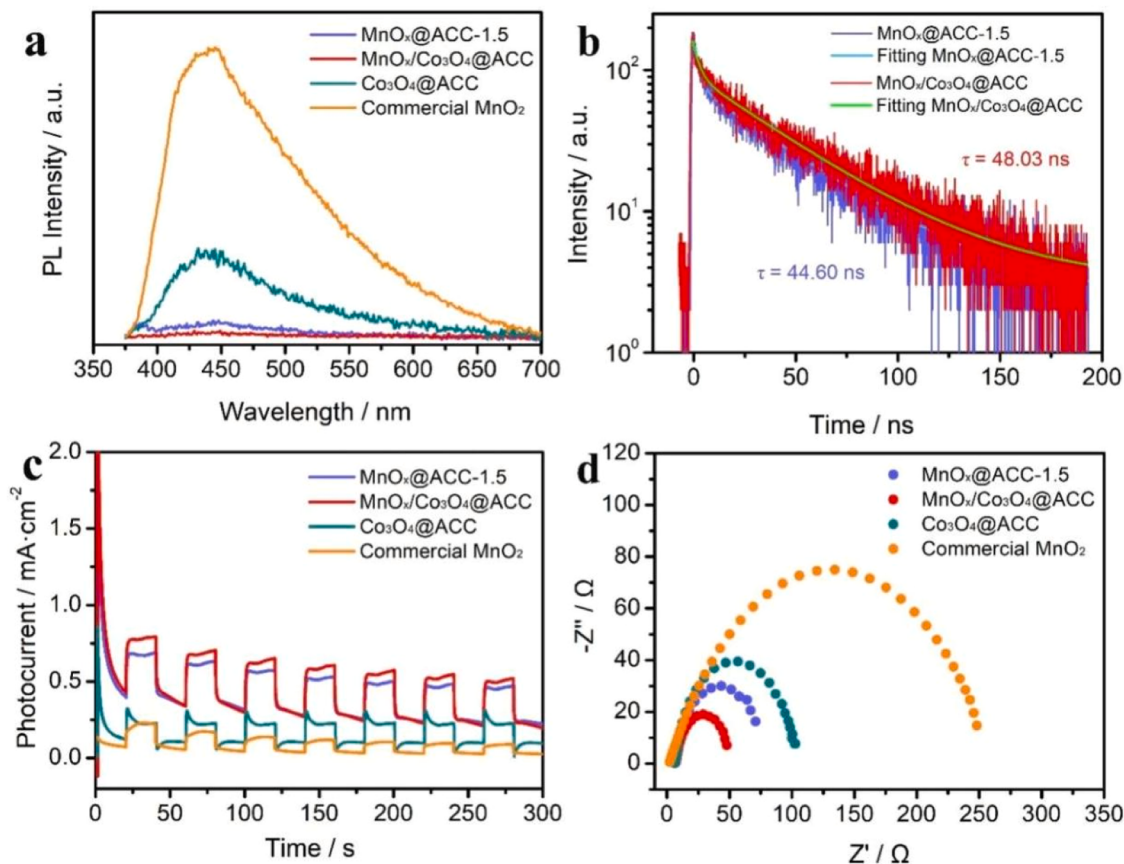


**Fig. 3.** (a) Photoluminescence spectra (PL), (b) the time-resolved fluorescence decay spectroscopy (TRPL) with excitation wavelength of 450 nm at 273.15 K under full spectrum irradiation, (c) transient photocurrents recorded, (d) EIS Nyquist plots of MnO<sub>x</sub>@ACC-1.5, MnO<sub>x</sub>/Co<sub>3</sub>O<sub>4</sub>@ACC, Co<sub>3</sub>O<sub>4</sub>@ACC, and Commercial MnO<sub>2</sub>.

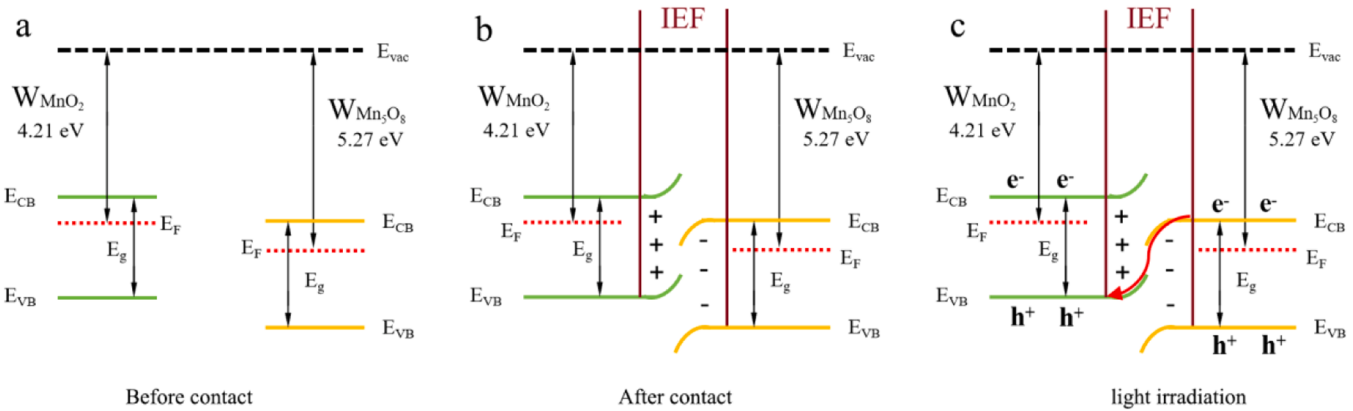


**Fig. 4.** The schematic diagram of charge transfer (a) before contact, (b) after contact, and (c) light illumination at MnO<sub>2</sub>/Mn<sub>5</sub>O<sub>8</sub> heterostructure interface.

interface (Fig. 4b). After photoexcitation, the VB electrons of MnO<sub>2</sub> and Mn<sub>5</sub>O<sub>8</sub> were quickly transferred to their CB. Driven by the interfacial IEF and bent bands, the photogenerated electrons in CB of Mn<sub>5</sub>O<sub>8</sub> spontaneously slid toward MnO<sub>2</sub> and recombined with the holes in VB of MnO<sub>2</sub> (Fig. 4c).

The valence state of elements and transfer direction of electrons were further comprehended by XPS. The survey spectrum (Fig. S25) displayed that the surfaces of MnO<sub>x</sub>@ACC-1.5 were mainly composed of Mn, O and C. As shown in Fig. 5a-b, compared with the pristine MnO<sub>x</sub>@ACC-1.1, the BEs of Mn 2p in MnO<sub>x</sub>@ACC-1.5 shifted from 640.01 eV (Mn<sup>II</sup>), 641.85 eV (Mn<sup>III</sup>) and 643.44 eV (Mn<sup>IV</sup>) to 640.14 eV, 642.06 eV and 643.51 eV in dark [30], indicating a reduction in electron density in MnO<sub>x</sub>@ACC-1.5. Conversely, the BEs of O 1s for MnO<sub>x</sub>@ACC-1.5

exhibited significant shifts to lower energy levels compared to that observed for MnO<sub>x</sub>@ACC-1.7, suggesting an increase in electron density after the formation of heterojunction. These results demonstrated that electrons residing on MnO<sub>2</sub> were effectively transferred to Mn<sub>5</sub>O<sub>8</sub> due to strong chemical interactions within the composite architecture. Notably, the BEs of Mn 2p in MnO<sub>x</sub>@ACC-1.5 composite was significantly shifted towards lower energy levels compared to its dark counterpart (Fig. 5a). However, the BEs of O 1s in the nanocomposite exhibited significant shifts to higher energy levels (Fig. 5b), indicating efficient transfer of photogenerated electrons from Mn<sub>5</sub>O<sub>8</sub> to MnO<sub>2</sub>. In conclusion, these XPS results provide crucial evidence for carrier transfer at MnO<sub>2</sub>/Mn<sub>5</sub>O<sub>8</sub> heterojunction interface under light irradiation. In the heterojunction formation process, the electronic transfer process at the interface was

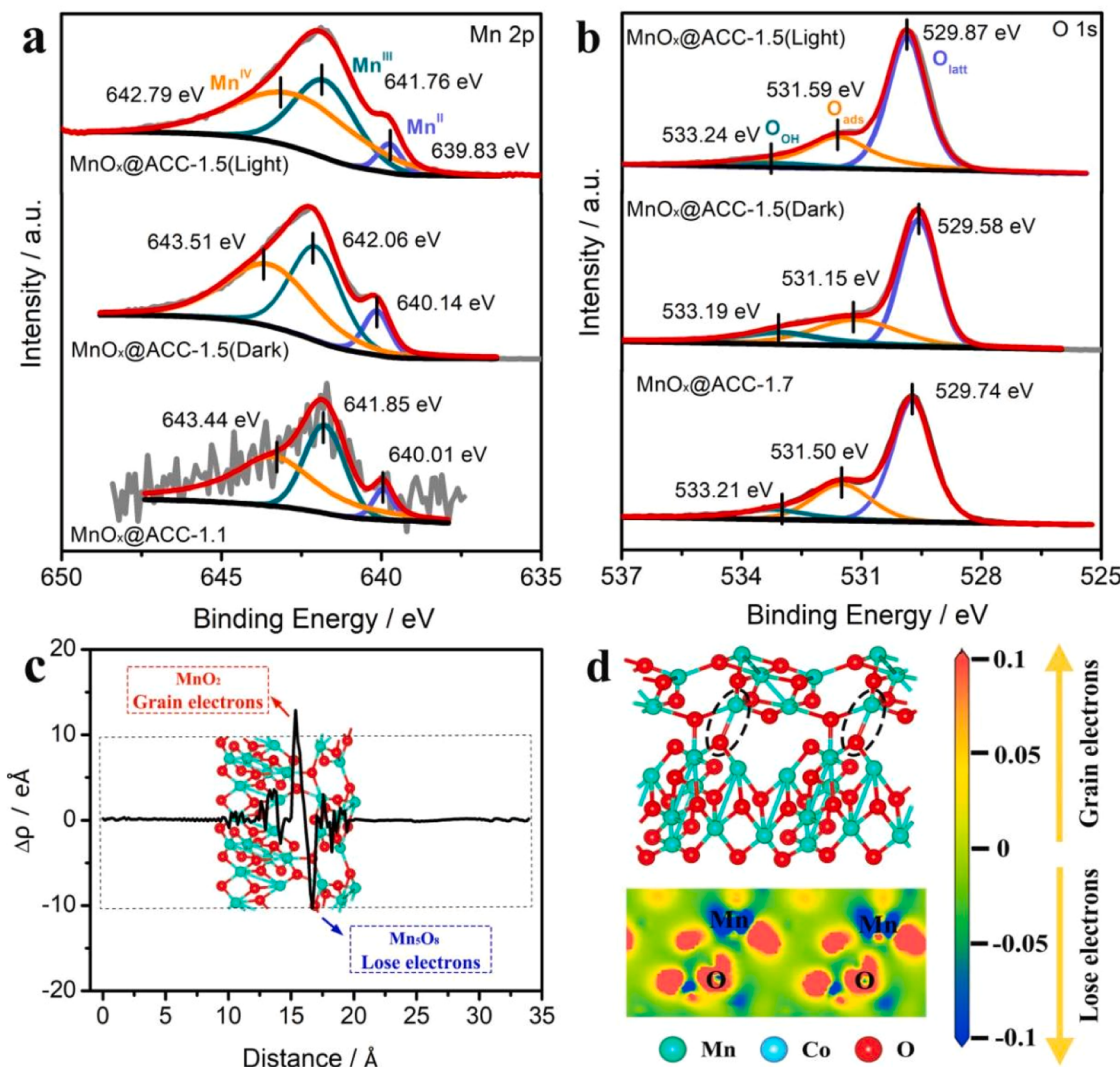


**Fig. 5.** In-situ XPS spectra of (a) Mn 2p, (b) O 1 s. (c) The electrons transfer process of MnO<sub>2</sub>/Mn<sub>5</sub>O<sub>8</sub> heterojunction. (d) the electron density difference of Mn–O bond slice.

investigated through Materials Studio (MS) script code (Fig. 5c). A strong interaction was formed at MnO<sub>2</sub>/Mn<sub>5</sub>O<sub>8</sub> interface after the formation of the heterojunction structure, indicating electrons transfer from Mn<sub>5</sub>O<sub>8</sub> to MnO<sub>2</sub> [31]. This conclusion was further confirmed by the electron density difference between the Mn–O bonded slices at the interface (Fig. 5d), where the blue and red regions represented electrons lose and grained in space, respectively. Our findings demonstrate that the electron transfer was enhanced due to the formation of the heterojunction structure at the MnO<sub>2</sub>/Mn<sub>5</sub>O<sub>8</sub> interface, ultimately enhancing catalytic activity.

After the introduction of Co<sub>3</sub>O<sub>4</sub>, the survey spectrum (Fig. S26) of MnO<sub>x</sub>/Co<sub>3</sub>O<sub>4</sub>@ACC are mainly composed of Mn, Co, O and C. The BEs of MnO<sub>x</sub>/Co<sub>3</sub>O<sub>4</sub>@ACC were higher than MnO<sub>x</sub>@ACC-1.5 in Mn 2p<sub>3/2</sub> (Fig. S27a), indicating that the stronger interaction was generated between MnO<sub>x</sub> and Co<sub>3</sub>O<sub>4</sub>. The fitting peaks position of Co 2p in MnO<sub>x</sub>/Co<sub>3</sub>O<sub>4</sub>@ACC shifted towards higher BEs compared to that of Co<sub>3</sub>O<sub>4</sub>@ACC [32], whilst the BEs of O 1 s in MnO<sub>x</sub>/Co<sub>3</sub>O<sub>4</sub>@ACC shifted towards lower energy levels compared to that observed for MnO<sub>x</sub>@ACC-1.5, suggesting that efficient transfer of photogenerated electrons from Co<sub>3</sub>O<sub>4</sub> to MnO<sub>x</sub> through Co–O bond (Fig. S25b–c). Such results also further confirmed that Co<sub>3</sub>O<sub>4</sub> favored the extraction of photogenerated holes from MnO<sub>x</sub>.

Based on the above analysis, the electron transfer scheme was plotted

in Fig. 6a. In this assembly, the photogenerated electrons produced by Mn<sub>5</sub>O<sub>8</sub> on CB and the photogenerated holes of MnO<sub>2</sub> on VB were combined. After the introduction of Co<sub>3</sub>O<sub>4</sub>, the photogenerated holes in Mn<sub>5</sub>O<sub>8</sub> surface were transferred to Co<sub>3</sub>O<sub>4</sub>. The high redox capacity of electrons and holes could be accumulated on CB of MnO<sub>2</sub> and VB of Co<sub>3</sub>O<sub>4</sub>, and then reacted with oxygen and water molecules adsorbed on the surface to produce highly active free radicals. The electron paramagnetic resonance (EPR) spectrum supported such electron transfer route. As shown in Fig. S28, the typical peak of DMOP·OH were not detected in the single MnO<sub>x</sub>@ACC-1.1, whereas the peak of DMOP·O<sub>2</sub> was observed, suggesting that MnO<sub>x</sub>@ACC-1.1 possessed a higher reduction potential under visible light excitation. However, the characteristic peak of DMOP·OH was observed but the peak of DMOP·O<sub>2</sub> was not detected in the single MnO<sub>x</sub>@ACC-1.7, indicating that MnO<sub>x</sub>@ACC-1.7 had strong oxidizing performance instead of reducing ability. For MnO<sub>x</sub>@ACC-1.5, the EPR signals of DMOP·OH and DMOP·O<sub>2</sub> were observed, validating its strong redox abilities owing to the Z-scheme heterojunction structure. Apparently, the photoexcited carriers were transferred through Z-scheme path. Similarly, after the introduction Co<sub>3</sub>O<sub>4</sub> into MnO<sub>x</sub>, the DMOP·OH signal of MnO<sub>x</sub>/Co<sub>3</sub>O<sub>4</sub>@ACC was significantly stronger than that of MnO<sub>x</sub>@ACC-1.5 under the irradiation for 10 min, indicating MnO<sub>x</sub>/Co<sub>3</sub>O<sub>4</sub>@ACC generated more electrons and exhibited stronger oxidizing capacity. However, there was no DMOP·

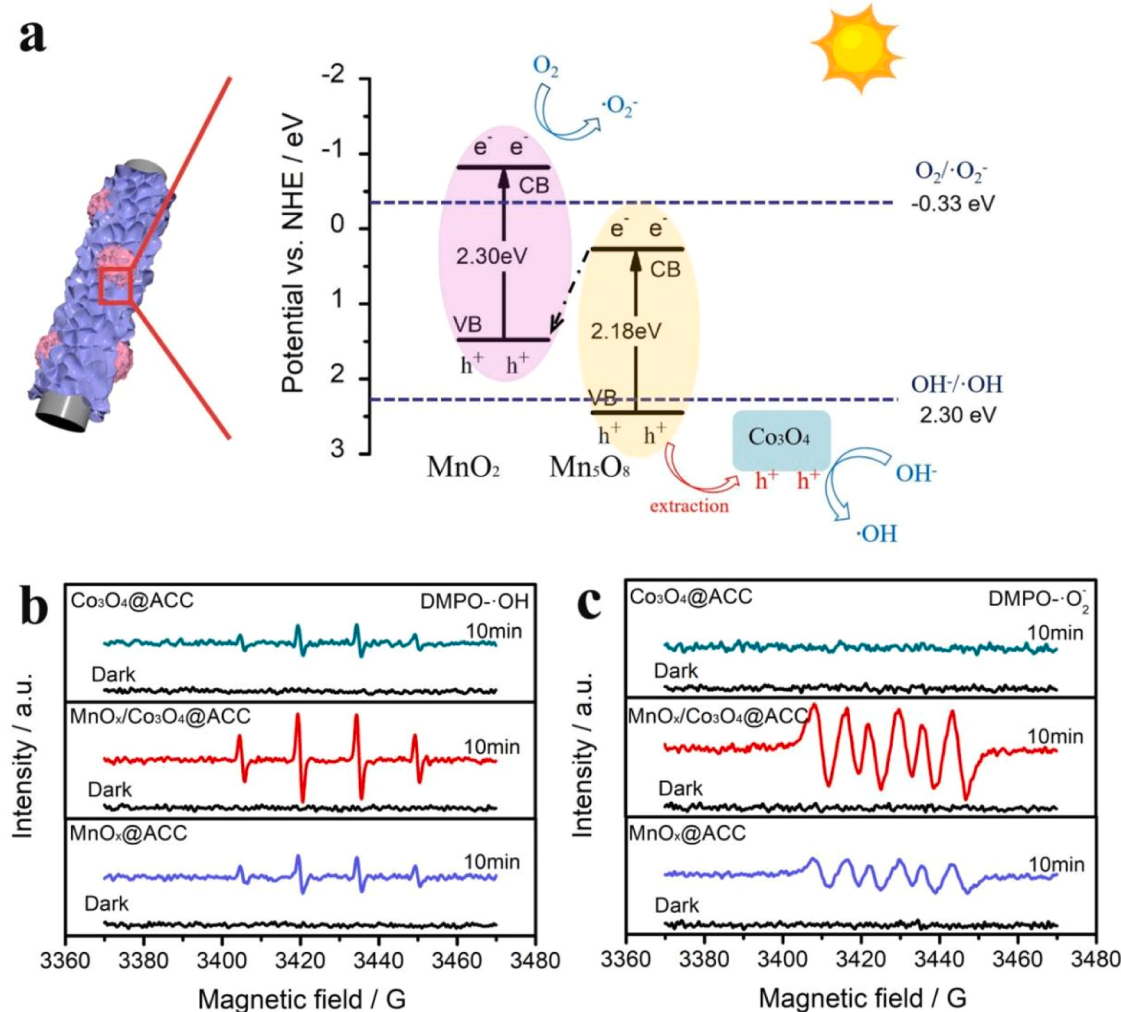


**Fig. 6.** (a) The diagram of the energy band arrangement and electron transfer in MnO<sub>x</sub>/Co<sub>3</sub>O<sub>4</sub> heterojunction. EPR spectra (in dark and light on 10 min) of (b) DMOP- ·OH and (c) DMOP- ·O<sub>2</sub> for MnO<sub>x</sub>@ACC-1.5, MnO<sub>x</sub>/Co<sub>3</sub>O<sub>4</sub>@ACC and Co<sub>3</sub>O<sub>4</sub>@ACC.

·O<sub>2</sub> signal and only a weak DMOP- ·OH after 10 min illumination on Co<sub>3</sub>O<sub>4</sub>@ACC, indicating that ·O<sub>2</sub> cannot be produced on Co<sub>3</sub>O<sub>4</sub>@ACC surface (Fig. 6b-c).

#### 3.4.3. Intermediate species and reaction routes

It has been experimentally proven that the introduction of Co<sub>3</sub>O<sub>4</sub> can effectively reduce CO generation. To further explore the relationship between catalysts and CO, the absorption models were used to investigate the adsorption of CO molecule on MnO<sub>x</sub>@ACC-1.5 and MnO<sub>x</sub>/Co<sub>3</sub>O<sub>4</sub>@ACC (Fig. 7a, b). The CO molecule tended to interact with O atom on the MnO<sub>x</sub>@ACC-1.5 surface, and the distance was shortened from 2.373 Å to 2.167 Å after structural optimization (Fig. S29). Additionally, the adsorption energy (E<sub>ads</sub>) of CO was -1.29 eV. Similarly, the distance between CO molecule and Co atom was shortened from 2.360 Å to 1.899 Å, and the E<sub>ads</sub> of CO was -1.50 eV in MnO<sub>x</sub>/Co<sub>3</sub>O<sub>4</sub>@ACC. Therefore, compared with MnO<sub>x</sub>@ACC-1.5, MnO<sub>x</sub>/Co<sub>3</sub>O<sub>4</sub>@ACC exhibited the shorter adsorption distance and the higher adsorption energy for CO molecule. The result indicated that CO was more easily absorbed on the surface of MnO<sub>x</sub>/Co<sub>3</sub>O<sub>4</sub>@ACC due to the introduction of Co<sub>3</sub>O<sub>4</sub>, and could be further oxidized [33].

In-situ diffuse reflexions infrared fourier transformations (DRIFT) was used to further analyze the surface adsorbed species and intermediates of benzene oxidation on MnO<sub>x</sub>@ACC-1.5 and MnO<sub>x</sub>/Co<sub>3</sub>O<sub>4</sub>@ACC in different reaction time under an unfiltered 300 W Xenon lamp irradiation. As shown in Fig. 7c, d, benzene reached saturated

adsorption, and six stable adsorption bands were detected at 0 min under room temperature. The adsorption bands at 1037, 1485 cm<sup>-1</sup> were assigned to C-H in-plane bending vibration and C-C skeleton stretching vibration of aromatic ring, respectively. The bands of 1814, 1957 cm<sup>-1</sup> and 3045, 3087 cm<sup>-1</sup> could be attributed to the combined frequency bands of C-H bending vibration and C-H stretching modes [34]. With the increase of irradiation time, the CO<sub>2</sub> vibration peaks at 2360, 2340 cm<sup>-1</sup> on the catalyst surface gradually enhanced [35], and some new peaks appeared. For MnO<sub>x</sub>@ACC-1.5, the two new peaks gradually enhanced at 1178, 1207 cm<sup>-1</sup> were ascribed to the C-O stretching vibrations [36], which might be caused by the accumulation of anhydride species on the catalyst surface. Besides, the band at 1542 cm<sup>-1</sup> was attributed to COOH stretching vibration of ethyl acetate surface [6]. For MnO<sub>x</sub>/Co<sub>3</sub>O<sub>4</sub>@ACC, the one at 1280 cm<sup>-1</sup> was assigned to slight carbonate species [37], and that at 1380 cm<sup>-1</sup> was ascribed to the CH<sub>3</sub> stretching vibrations of acetic acid species [37]. The band at 1585 cm<sup>-1</sup> was attributable to the C=C stretching vibrations of phenolate species [37]. The band at 1685 cm<sup>-1</sup> was assigned to o-quinone [38] and the peaks of free water were obviously seen at 3600–3750 cm<sup>-1</sup>. In addition, the weak CO vibration peaks at 2182 cm<sup>-1</sup> was detected [37]. Therefore, MnO<sub>x</sub>/Co<sub>3</sub>O<sub>4</sub>@ACC could deeply oxidize gaseous benzene than MnO<sub>x</sub>@ACC-1.5. Taken together these results, the reaction path of gaseous benzene oxidation was supposed to followed as benzene → phenolate → o-quinone → acetic acid → carbonate → CO → CO<sub>2</sub> and H<sub>2</sub>O.

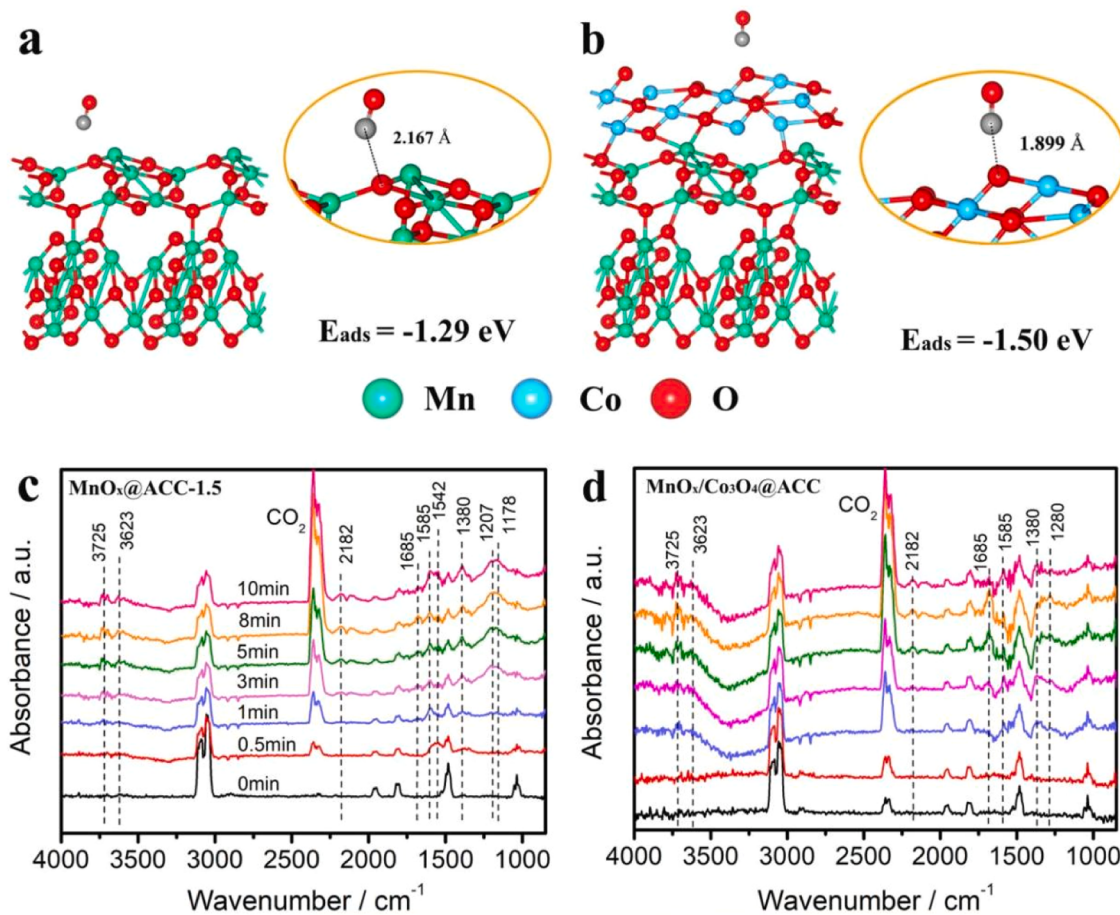


**Fig. 7.** The CO absorption geometric structure of (a)  $\text{MnO}_x@\text{ACC}$ , (b)  $\text{MnO}_x/\text{Co}_3\text{O}_4@\text{ACC}$ . In-situ DRIFT spectra of (c)  $\text{MnO}_x@\text{ACC}-1.5$ , (d)  $\text{MnO}_x/\text{Co}_3\text{O}_4@\text{ACC}$  under 80 %  $\text{N}_2$  + 20 %  $\text{O}_2$  during benzene oxidation process at different irradiation time.

#### 3.4.4. Environmental application potential

The  $\text{MnO}_x/\text{Co}_3\text{O}_4@\text{ACC}$  photocatalyst demonstrated excellent photocatalytic activity, mineralization and stability in benzene degradation. To further assess the application potential of the  $\text{MnO}_x/\text{Co}_3\text{O}_4@\text{ACC}$  in volatile organic compounds (VOCs) degradation, toluene, acetaldehyde and formaldehyde were also tested and compared with benzene. The degradation efficiency above 99 % can be achieved for all studied compounds (Fig. S30). Furthermore, with its high stability after 60 cycles (30 h), the approximate treatment scales of  $\text{MnO}_x/\text{Co}_3\text{O}_4@\text{ACC}$  photocatalyst ( $4 \text{ m}^2$ ) were estimated to be  $31.2\text{--}40.8 \text{ m}^3/\text{d}$ ,  $34.7\text{--}45.3 \text{ m}^3/\text{d}$ ,  $52.0\text{--}68.0 \text{ m}^3/\text{d}$  and  $62.4\text{--}81.6 \text{ m}^3/\text{d}$  for benzene, toluene, acetaldehyde and formaldehyde, respectively, according to conversion factor (0.65–0.85) [38,39]. In the economic point of view, photocatalytic oxidation exhibited cost-effective profiles for removing VOCs from the environment. Compared to other traditional technologies (Table S6), higher removal efficiency and mineralization rate with lower energy consumption and cost can be achieved using photocatalytic. In present work, the estimated costs were \$1.74, \$2.06, \$0.98, \$0.67 for removing per gram benzene, toluene, acetaldehyde and formaldehyde, respectively. In addition, the  $\text{MnO}_x/\text{Co}_3\text{O}_4@\text{ACC}$  photocatalyst demonstrates broad adaptability for integration into a wide array of application scenarios, due to the inherent softness and cutability of carbon cloth. This adaptability specific operational environments promise significant reductions in operational costs. Concurrently, the deposited samples exhibited strong adhesion to the surface of carbon cloth, thereby reducing the secondary pollution risk. The use of solar radiation as the exclusive energy source for industrial applications, especially considering its VOCs degradation rate and net-zero energy footprint.

#### 4. Conclusions

In summary, a possible photocatalytic mechanism of gaseous benzene is proposed based on the above experimental results and DFT theoretical analysis (Fig. 8).  $\text{MnO}_x$  and  $\text{Co}_3\text{O}_4$  are sculptured layer by layer on the ACC surface to form  $\text{MnO}_x/\text{Co}_3\text{O}_4@\text{ACC}$  at the interface. In this assembly, a strong internal electric field is created in highly coupled  $\text{MnO}_2/\text{Mn}_5\text{O}_8$  on ACC surface, which can greatly facilitate the separation and transmission of photogenerated carriers. After the introduction of  $\text{Co}_3\text{O}_4$ , the photogenerated holes in  $\text{MnO}_x$  surface are transferred to  $\text{Co}_3\text{O}_4$  surface to avoid photocorrosion caused by the oxidation from  $\text{Mn}^{II}$  and  $\text{Mn}^{III}$ . Therefore, the accumulated electrons in  $\text{MnO}_2$  and holes in  $\text{Co}_3\text{O}_4$  react with oxygen and water molecules absorbed on the catalyst surface to form active oxygen species ( $\cdot\text{O}_2^-$  and  $\cdot\text{OH}$ ), which oxidize benzene to  $\text{H}_2\text{O}$  and  $\text{CO}_2$ . Additionally, CO molecules are easily absorbed on  $\text{MnO}_x/\text{Co}_3\text{O}_4@\text{ACC}$  surface to further activate. In short, the highly coupled transition metal oxides on the ACC, the separation and transmission of photogenerated electron-holes, the benign hole trapping ability of  $\text{Co}_3\text{O}_4$ , CO adsorption and activation are responsible for the rapid degradation and excellent stability of gaseous benzene.

#### CRediT authorship contribution statement

**Yuanqing Tang:** Software, Data curation, Conceptualization. **Xinyue Jiang:** Validation, Formal analysis. **Yangzheng Liu:** Validation, Methodology, Formal analysis. **Zhongli Wang:** Writing – review & editing, Supervision, Investigation, Formal analysis, Conceptualization. **Xiaojing Wang:** Writing – review & editing, Supervision. **Fei Xie:** Validation, Software, Conceptualization. **Lili Wan:** Writing – review &

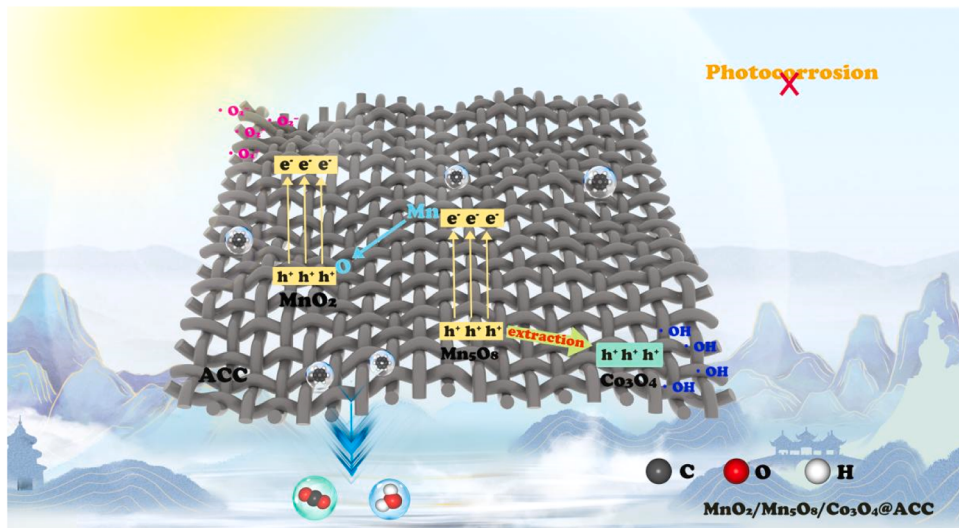


**Fig. 8.** Schematic illustration of the photocatalytic benzene degradation for  $\text{MnO}_x/\text{Co}_3\text{O}_4@\text{ACC}$ .

editing, Methodology, Conceptualization. **Liang Qi:** Writing – original draft, Software, Methodology, Investigation, Formal analysis, Conceptualization. **Changwei Lü:** Writing – review & editing, Validation, Supervision, Conceptualization.

#### Declaration of Competing Interest

The authors declare that they have no known competing financial interests or personal relationships that could have appeared to influence the work reported in this paper.

#### Data Availability

Data will be made available on request.

#### Acknowledgements

This research is supported by the National Natural Science Foundation of China (42167028, 22366028, 22062016), the Project of the Key Science and Technology of Inner Mongolia of China (2021GG0110), the Higher Education Reform and Development Project of Inner Mongolia University (11200-121028). We would like to thank School of Chemistry and Chemical Engineering of Inner Mongolia University for EPR test and Shiyanjia Lab ([www.shiyanjia.com](http://www.shiyanjia.com)) for XPS, SEM, TEM and TRPL tests.

#### Appendix A. Supporting information

Supplementary data associated with this article can be found in the online version at [doi:10.1016/j.apcatb.2024.124099](https://doi.org/10.1016/j.apcatb.2024.124099).

#### References

- [1] R.A. Harley, D.S. Hooper, A.J. Kean, T.W. Kirchstetter, J.M. Hesson, N.T. Balberan, E.D. Stevenson, G.R. Kendall, Effects of reformulated gasoline and motor vehicle fleet turnover on emissions and ambient concentrations of benzene, *Environ. Sci. Technol.* 40 (2006) 5084–5088.
- [2] S. Wi, M.G. Kim, S.W. Myung, Y.K. Baik, S. Kim, Evaluation and analysis of volatile organic compounds and form aldehyde emission of building products in accordance with legal standards: a statistical experimental study, *J. Hazard. Mater.* 393 (2020) 122381.
- [3] G. Wang, S. Cheng, W. Wei, Y. Zhou, S. Yao, H. Zhang, Characteristics and source apportionment of VOCs in the suburban area of Beijing, China, *Atmos. Pollut. Res.* 7 (2016) 711–724.
- [4] M. Sun, D. Li, Y. Zheng, W. Zhang, Y. Shao, Y. Chen, W. Li, X. Fu, Microwave hydrothermal synthesis of calcium antimony oxide hydroxide with high photocatalytic activity toward benzene, *Environ. Sci. Technol.* 43 (2009) 7877–7882.
- [5] B. Borjigin, L. Ding, H. Li, X. Wang, A solar light-induced photo-thermal catalytic decontamination of gaseous benzene by using  $\text{Ag}/\text{Ag}_3\text{PO}_4/\text{CeO}_2$  heterojunction, *Chem. Eng. J.* 402 (2020) 126070.
- [6] Q. Zhao, Y. Zheng, C. Song, Q. Liu, N. Ji, D. Ma, X. Lu, Novel monolithic catalysts derived from in-situ decoration of  $\text{Co}_3\text{O}_4$  and hierarchical  $\text{Co}_3\text{O}_4@\text{MnO}_x$  on Ni foam for VOC oxidation, *Appl. Catal. B Environ. Energy* 265 (2020) 118552.
- [7] B. Yang, B. Guan, Synergistic catalysis of ozonation and photooxidation by sandwich structured  $\text{MnO}_2-\text{NH}_2/\text{GO}/\text{p-C}_3\text{N}_4$  on cephalexin degradation, *J. Hazard. Mater.* 439 (2022) 129540.
- [8] J. Zhao, N. Li, R. Yu, Z. Zhao, J. Nan, Magnetic field enhanced denitrification in nitrate and ammonia contaminated water under 3D/2D  $\text{Mn}_2\text{O}_3/\text{g-C}_3\text{N}_4$  photocatalysis, *Chem. Eng. J.* 349 (2018) 530–538.
- [9] S. Das, A. Samanta, S. Jana, Light-assisted synthesis of hierarchical flower-Like  $\text{MnO}_2$  nanocomposites with solar light induced enhanced photocatalytic activity, *ACS Sustain. Chem. Eng.* 5 (2017) 9086–9094.
- [10] J. Zhao, J. Nan, Z. Zhao, N. Li, J. Liu, F. Cui, Energy-efficient fabrication of a novel multivalence  $\text{Mn}_3\text{O}_4-\text{MnO}_2$  heterojunction for dye degradation under visible light irradiation, *Appl. Catal. B Environ. Energy* 202 (2017) 509–517.
- [11] R. Tao, X. Qu, Z. Wang, F. Li, L. Yang, J. Li, D. Wang, K. Zheng, M. Dong, Tune the electronic structure of  $\text{MoS}_2$  heterojunction for broadband photodetection, *J. Mater. Sci. Technol.* 119 (2022) 61–68.
- [12] T. Zhao, B. Li, C. Wang, S. Wu, S. Zhu, H. Jiang, Y. Zheng, Z. Li, Z. Cui, Y. Zhang, P. Chu, X. Liu, Tuning the bandgap of  $\text{MnO}_2$  heterojunction by building active high-index facet to achieve rapid electron transfer for enhanced photocatalytic sterilization, *J. Mater. Sci. Technol.* 168 (2023) 265–275.
- [13] K. Seki, T. Higashi, Y. Kawase, K. Takanabe, K. Domen, Exploring the photocorrosion mechanism of a photocatalyst, *J. Phys. Chem. Lett.* 13 (2022) 10356–10363.
- [14] T.J. Macdonald, A.J. Clancy, W. Xu, Z. Jiang, C. Lin, L. Mohan, T. Du, D.D. Tune, Phosphorene nanoribbon-augmented optoelectronics for enhanced hole extraction, *J. Am. Chem. Soc.* 143 (2021) 21549–21559.
- [15] B. Chen, D. Li, X. Wu, S. Deng, L. Li, W. Shi, Ultrathin black phosphorus as a pivotal hole extraction layer and oxidation evolution co-catalyst boosting solar water oxidation, *Inorg. Chem. Front.* 9 (2022) 2938–2944.
- [16] Y. Zhou, X. Zhang, X. Lu, X. Gao, J. Gao, L. Shui, S. Wu, Promoting the hole extraction with  $\text{Co}_3\text{O}_4$  nanomaterials for efficient carbon-based  $\text{CsPbI}_2\text{Br}$  perovskite solar cells, *Sol. RRL* 3 (2019) 1800315.
- [17] K. Lu, Y. Gao, Z. Wang, X. Wang, H. Meng, Efficient hole extraction and dark current suppression in organic photodetectors enabled by atomic-layer-deposition of ultrathin  $\text{Co}_3\text{O}_4$ , *Inter. J. Mater. Chem. C* 11 (2023) 8600–8608.
- [18] K. Yu, T. Zhang, Y. Wang, J. Wu, H. Huang, K. Yin, F. Liao, F. Liao, Y. Liu, Z. Kang, Anchoring  $\text{Co}_3\text{O}_4$  on  $\text{CdZnS}$  to accelerate hole migration for highly stable photocatalytic overall water splitting, *Appl. Catal. B Environ. Energy* 324 (2022) 122228.
- [19] D. Zu, H. Song, Y. Wang, Z. Chao, Z. Li, G. Wang, Y. Shen, C. Li, J. Ma, One-pot in-situ hydrothermal synthesis of  $\text{CdS}/\text{Nb}_2\text{O}_5/\text{Nb}_2\text{C}$  heterojunction for enhanced visible-light-driven photodegradation, *Appl. Catal. B Environ. Energy* 277 (2020) 119140.
- [20] X. Wen, Q. Lu, X. Lv, J. Sun, J. Guo, Z. Fei, C. Niu, Photocatalytic degradation of sulfamethazine using a direct Z-Scheme  $\text{AgI}/\text{Bi}_2\text{V}_2\text{O}_{11}$  photocatalyst: Mineralization activity, degradation pathways and promoted charge separation mechanism, *J. Hazard. Mater.* 385 (2020) 121508.
- [21] W. Guo, H. Luo, Z. Jiang, W. Shangguan, In-situ pressure-induced  $\text{BiVO}_4/\text{Bi}_{0.6}\text{Y}_{0.4}\text{VO}_4$  S-scheme heterojunction for enhanced photocatalytic overall water splitting activity, *Chin. J. Catal.* 43 (2022) 316–328.

[22] J. Tao, J. Jiang, S. Zhao, Y. Zhang, X. Li, X. Fang, P. Wang, W. Hu, Y.H. Lee, H. Lu, Fabrication of 1D Te/2D  $\text{ReS}_2$  mixed-dimensional van der waals p-n heterojunction for high-performance phototransistor, *ACS Nano* 15 (2021) 3241–3250.

[23] J. Li, S. Luo, B. Zhang, J. Lu, W. Liu, Q. Zeng, J. Wan, X. Han, C. Hu, High-performance asymmetric  $\text{Mn(OH)}_2//\text{Fe}_2\text{O}_3$  supercapacitor achieved by enhancing and matching respective properties of cathode and anode materials, *Nano Energy* 79 (2021) 105410.

[24] X. Shen, T. Zhang, P. Xu, L. Zhang, J. Liu, Z. Chen, Growth of  $\text{C}_3\text{N}_4$  nanosheets on carbon-fiber cloth as flexible and macroscale filter-membrane-shaped photocatalyst for degrading the flowing wastewater, *Appl. Catal. B Environ. Energy* 219 (2017) 425–431.

[25] C. Revathi, R.T.R. Kumar, Electro catalytic properties of  $\alpha$ ,  $\beta$ ,  $\gamma$ ,  $\epsilon$ - $\text{MnO}_2$  and  $\gamma$ - $\text{MnOOH}$  nanoparticles: Role of polymorphs on enzyme free  $\text{H}_2\text{O}_2$  sensing, *Electroanalysis* 29 (2017) 1481–1489.

[26] A. Maity, S.S. Ray, Synthesis of  $\text{Co}_3\text{O}_4/\text{poly}(\text{N-vinylcarbazole})$  core/shell composite with enhanced optical property, *Macromol. Mater. Eng.* 295 (2010) 153–158.

[27] X. Hao, Y. Wang, J. Zhou, Z. Cui, Y. Wang, Z. Zou, Zinc vacancy-promoted photocatalytic activity and photostability of  $\text{ZnS}$  for efficient visible-light-driven hydrogen evolution, *Appl. Catal. B Environ. Energy* 221 (2018) 302–311.

[28] J. Zheng, L. Zhang, Incorporation of  $\text{CoO}$  nanoparticles in 3D marigold flower-like hierarchical architecture  $\text{MnCo}_2\text{O}_4$  for highly boosting solar light photo-oxidation and reduction ability, *Appl. Catal. B Environ. Energy* 237 (2018) 1–8.

[29] T. Liu, K. Yang, H. Gong, Z. Jin, Visible-light driven S-scheme  $\text{Mn}_{0.2}\text{Cd}_{0.8}\text{S}/\text{CoTiO}_3$  heterojunction for photocatalytic hydrogen evolution, *Renew. Energy* 173 (2021) 389–400.

[30] W. Yang, Y. Peng, Y. Wang, Y. Wang, H. Liu, Z. Su, W. Yang, J. Chen, W. Si, J. Li, Controllable redox-induced in-situ growth of  $\text{MnO}_2$  over  $\text{Mn}_2\text{O}_3$  for toluene oxidation: active heterostructure interfaces, *Appl. Catal. B Environ. Energy* 278 (2020) 119279.

[31] N. Li, X. Chen, J. Wang, X. Liang, L. Ma, X. Jing, D. Chen, Z. Li,  $\text{ZnSe}$  nanorods– $\text{CsSnCl}_3$  perovskite heterojunction composite for photocatalytic  $\text{CO}_2$  reduction, *ACS Nano* 16 (2022) 3332–3340.

[32] P. Shi, X. Dai, H. Zheng, D. Li, W. Yao, C. Hu, Synergistic catalysis of  $\text{Co}_3\text{O}_4$  and graphene oxide on  $\text{Co}_3\text{O}_4/\text{GO}$  catalysts for degradation of Orange II in water by advanced oxidation technology based on sulfate radicals, *Chem. Eng. J.* 240 (2014) 264–270.

[33] J. Bae, D. Shin, H. Jeong, B.S. Kim, J.W. Han, H. Lee, Highly water-resistant La-doped  $\text{Co}_3\text{O}_4$  catalyst for CO oxidation, *ACS Catal.* 9 (2019) 10093–10100.

[34] D. Ma, L. Yang, Z. Sheng, Y. Chen, Photocatalytic degradation mechanism of benzene over  $\text{ZnWO}_4$ : Revealing the synergistic effects of Na-doping and oxygen vacancies, *Chem. Eng. J.* 405 (2021) 126538.

[35] J. Yao, F. Dong, H. Feng, Z. Tang, Hierarchical  $\text{MnO}_x/\text{Co}_3\text{O}_4$  nanoarrays on Ni foam for catalytic oxidation of volatile organic compounds, *ACS Appl. Nano Mater.* 4 (2021) 9322–9332.

[36] L. Xiong, Z. Sun, X. Zhang, L. Zhao, P. Huang, X. Chen, H. Jin, H. Sun, Y. Lian, Z. Deng, Y. Peng, Octahedral gold-silver nanoframes with rich crystalline defects for efficient methanol oxidation manifesting a CO-promoting effect, *Nat. Commun.* 10 (2019) 3782.

[37] J.H. Lee, H. Jang, J.H. Kim, J.H. Park, K.Y. Lee, M.B. Park, S.B. Kang, T. Chang, L. Heo, Low temperature benzene oxidation over copper-silver catalyst: roles of copper oxide and silver on cerium-zirconium mixed oxide, *Catal. Sci. Technol.* 10 (2020) 6780–6789.

[38] Z. Li, W. Shen, J.P. Corriou, X. Chen, H. Xi, Assessment of multiple environmental factors on the adsorptive and photocatalytic removal of gaseous formaldehyde by a nano- $\text{TiO}_2$  colloid: experimental and simulation studies, *J. Colloid Interface Sci.* 608 (2022) 1769–1781.

[39] B. Li, Z. Cheng, R. Yao, H. Wang, W. Yu, Z. Bu, J. Xiong, T. Zhang, E. Essah, H. Kipen, An investigation of formaldehyde concentration in residences and the development of a model for the prediction of its emission rates, *Build. Environ.* 147 (2019) 540–550.